Surface & Coatings Technology 496 (2025) 131594

Contents lists available at ScienceDirect

Surface & Coatings Technology

journal homepage: www.elsevier.com/locate/surfcoat

High temperature properties of nichrome resistant heaters – A systematic comparison of APS, suspension and filament HVOF sprayed coatings

Marvin Sauter [a,*], Christian Semmler [a], Tobias Nies [a], Giulia Poppi [b], Luca Bortolotti [b], Filippo Ottani [b], Giovanni Bolelli [b], Luca Lusvarghi [b], Andreas Killinger [a]

[a] Institut für Fertigungstechnologien keramischer Bauteile (IFKB), Universität Stuttgart, Allmandring 7b, D-70569 Stuttgart, Germany
[b] Dipartimento di Ingegneria Enzo Ferrari, Università di Modena e Reggio Emilia, Via Pietro Vivarelli 10, I-41125 Modena, Italy

ARTICLE INFO

Keywords:
Resistance heating
HVOF
Plasma spraying
Nickel-chromium alloy (Ni20Cr)
High temperature

ABSTRACT

This study investigates the performance of Nichrome coatings, a nickel-chromium alloy containing 20 wt.-% chromium, applied using three thermal spray techniques: powder plasma spray, suspension HVOF, and filament HVOF. Thin, homogeneous coatings approximately 35 μm thick were deposited onto steel substrates pre-coated with an insulating Al_2O_3 layer. The oxide content in the coatings varied based on the spraying technique and parameters, ranging from 57 to 64 vol.-% for plasma spraying, 42 to 54 vol.-% for filament HVOF, and 9 to 43 vol.-% for suspension HVOF. The coating's heating performance was evaluated over a temperature range of room temperature (RT) to 700 °C. Analytical techniques such as X-ray Diffraction (XRD), Scanning Electron Microscopy (SEM), and Energy Dispersive X-ray Spectroscopy (EDS) were employed to investigate the mechanisms affecting temperature-dependent resistivity in relation to the coating microstructure. The results indicate that increased oxidation leads to a decrease in specific resistivity at RT (ρ_0). In example, plasma sprayed coatings exhibited lower specific resistivity ρ_0 of 0.80 $\Omega mm^2/m$. In contrast, suspension HVOF reaches values up to 2.75 $\Omega mm^2/m$. At the same time coatings with higher oxidation levels demonstrate an elevated dependence of resistivity as compared to less oxidized coatings. Both can be attributed to changes in the phase composition of the conductive phase as the dominating factor, primarily driven by the preferential oxidation of chromium during the spraying process. Notably, the results provide valuable information for adjusting the coating properties to suit specific needs, such as self-regulating or high-temperature heating applications.

1. Introduction

Transitioning from fossil fuels to renewable electric energy presents challenges, especially when considering the global CO_2 reduction objectives of achieving net zero between 2050 and 2060 as stated by the Intergovernmental Panel on Climate Change (IPCC) [1]. This shift impacts various industrial sectors, including those reliant on high-temperature processes, such as catalytic reactors for hydrogen production, where temperatures of up to 900 °C are needed [2]. One method to achieve these temperatures is through resistance heating in reactors that are currently heated using fossil fuel gas. [3,4] A notable material for resistant heater coatings is Nichrome, as for example Ni20Cr, recognized for its high-temperature oxidation and corrosion resistance attributed to the formation of a protective Cr_2O_3 layer [5–9]. For applying resistant heater coatings, thermal spraying emerges as a viable option, allowing flexibility in design, whether areal or structural, and accommodating materials ranging from various metals and alloys, metal matrix composites to oxides [10–15]. Traditional techniques like Wire Arc Spraying (WAS), Atmospheric Plasma Spraying (APS) and High Velocity Oxy Fuel Spraying (HVOF) have constraints, primarily limited due to large splat size, causing a high surface roughness, coarse microstructure and high variation in coating thickness [16–19]. Therefore, classical methods are limited to coatings >30 μm, since irregularities cause hot spot formation and possibly lead to coating failure [20]. In contrast, suspension-based or filament-based methods facilitate the application of finer particles and therefore finer microstructures with lower roughness and less inhomogeneities, enabling thinner coatings [21–26]. As a result, more diverse design possibilities are feasible, which can be crucial in confined spaces and for large contiguously coated areas. The properties of the coating, including resistivity, temperature coefficient of resistance (TCR), and uniform thickness, significantly influence the heating element's performance [27,28]. Thus, optimizing both coating and

---

* Corresponding author.
E-mail address: marvin.sauter@ifkb.uni-stuttgart.de (M. Sauter).

https://doi.org/10.1016/j.surfcoat.2024.131594
Received 7 October 2024; Received in revised form 18 November 2024; Accepted 23 November 2024

geometric properties is essential for energy-efficient heating systems [29]. Achieving high efficiency necessitates adjusting the heating elements resistance according to the power supply and desired temperature. However, understanding coating properties is intricate with factors like resistivity, microstructure, phase composition, oxide content and TCR interplaying to define the materials characteristics [30–32]. Limited data exists on suspension HVOF coatings, and no data are available on filament HVOF coating yet as it is a new technology [22,33,34]. Most published studies of Ni20Cr coatings focus on temperatures of maximum 400 °C [33,34], or in a singular case on a maximum of 600 °C [35] emphasizing the need for comprehensive studies in the high temperature regime. This research endeavours to systematically assess Nichrome coatings produced through advanced techniques like suspension and filament HVOF, comparing them to state-of-the-art plasma sprayed coatings used for industrial applications. The objective is to determine the potential and suitable fields of applications of each method in the context of renewable energy transition.

2. Experimental procedure

2.1. Coating procedure

Resistant heater elements have been fabricated using a 100x100x3 mm steel substrate as base material. On top of the substrate three functional coatings were applied. The initial layer comprises a 150 µm thick Al_2O_3 insulation coating applied by APS, designed to avoid electrical contact of the contacted surface and the steel substrate. Subsequently, a 30–40 µm thick conductive meander shaped Nichrome coating is applied serving as the functional coating used for heating. The meander width was set to 5 mm and the overall path length was 549 mm. Lastly, a suspension HVOF sprayed copper layer is selectively applied exclusively to the contact regions at the extremities of the meandering structure, aiming to minimize contact resistance during power supply interfacing. To confine the coated area to the desired shape, 2 mm thick steel masks were employed. An in-plane and a side view of the element is depicted in Fig. 1.

Prior to applying the Al_2O_3 layer, the steel substrate underwent preparation with F60 corundum grit blasting at a pressure of 5 bar, followed by sequential degreasing using acetone. Subsequent layers of Nichrome and Cu were directly applied onto the pre-existing coating after meticulous removal of overspray and possible contaminants. The coating parameters of the Al_2O_3 and Cu layers are not discussed in more detail. The resistant heater coatings were applied using three distinct spraying techniques, namely filament and suspension HVOF using the TopGun system (GTV Verschleißschutz, Germany) and APS using the F6 torch (GTV Verschleißschutz, Germany). In case of suspension and filament HVOF a 22-8-78 and 12-8-78 nozzle were employed, respectively. For each spraying technique three sets of parameters were used for the Nichrome coating with the goal to adjust the oxide content within the coating, yielding a total of nine samples. In the case of filament and suspension HVOF the stoichiometric ratio λ was varied between 0.6 and 0.8, while the spraying distance d for APS ranged between 120 and 200 mm. All other parameters remained constant. A detailed list of all parameters is given in Table 1. Note that the feed rate relates to the net powder delivered, excluding water and polymer in case of HVOF. The torch path was set to a meander pattern with a torch speed of 800 mm/s for HVOF and 500 mm/s for APS.

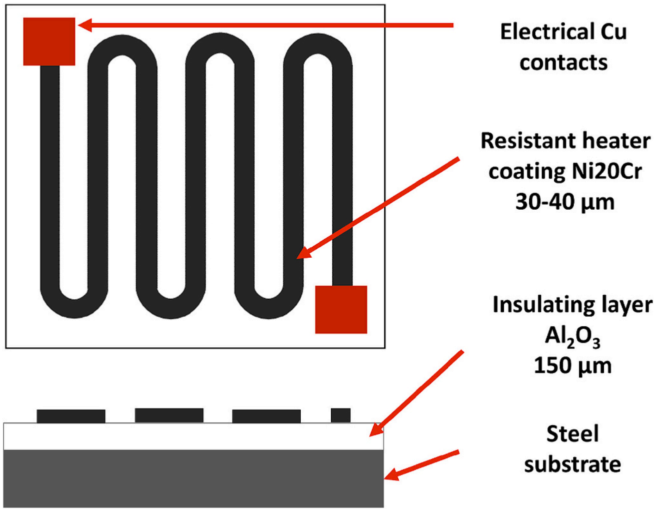

Fig. 1. Schematic of the resistant heater element geometry and build-up.

The parameters for APS are based on coatings for industrial application. A fine −25 + 5 µm Ni20Cr powder (251.071, Höganäs, Sweden) was selected to ensure a uniform thickness distribution and microstructure within the targeted coating thickness of 30 to 40 µm. For filament and suspension HVOF techniques, a −12 + 5 µm Ni20Cr (251.051, Höganäs, Sweden) was dispersed in a suspension and a filament, respectively. The aqueous suspension was prepared to have a powder content of 15 wt.-% and was stabilized adding 1.5 wt.-% of hydrocolloid flow aid. First, the powder was slowly added to deionized water while the mixture was stirred at 2000 rpm using a disperser (Dispermat, VMA Getzmann, Germany). Second, the hydrocolloid was added, before the mixture was dispersed for 30 min at 3200 rpm to ensure a homogenous distribution and disintegration of any agglomerates. The filament was created in a two-step process. In a first step, the dried polypropylene granules (H120 GP / 3, Sibur International, Austria) and Ni20Cr powder were processed into homogenous granules using a twin-screw extruder EBVP25 (O.M.C., Italy). Gravimetric dosing was used to set the desired mass fraction of the powder to 86.5 wt.-%. In a second step, the compounded granules were remolten using a single screw extruder 30x25D (Collin, Germany) and drawn into a filament with 1.5 mm in diameter.

2.2. Feedstock and coating characterization

The particle size distributions (PSD) of the feedstock materials were analysed by laser diffraction in aqueous suspension utilizing a Mastersizer 3000 (Malvern, United Kingdom). The suspension for suspension HVOF and the raw powder for APS were measured as processed, whereas the raw powder was measured for filament HVOF

Table 1
Overview of spraying parameters of APS, suspension-based and filament based HVOF.

APS samples	d [mm]	I [A]	H_2 / Ar [slpm]	Passes	Feed rate [g/min]
APS120	120	550	6 / 45	2	18.4
APS160	160				
APS200	200				
Suspension HVOF	**d [mm]**	**λ**	**$C_2H_4 + O_2$ [slpm]**	**Passes**	**Feed rate [g/min]**
S0.6	110	0.6	200	5	9.0
S0.7		0.7			
S0.8		0.8			
Filament HVOF	**d [mm]**	**λ**	**$C_2H_4 + O_2$ [slpm]**	**Passes**	**Feed rate [g/min]**
F0.6	110	0.6	200	6	9.1
F0.7		0.7			
F0.8		0.8			

representative for the filament feedstock. Microstructure cross-sections of the filament and the coatings were investigated by means of light microscopy (LM) and scanning electron microscopy (SEM) using a Fischerscope H100 (Helmut Fischer, Germany) and Nova NanoSEM 450 (FEI – Thermo Fisher Scientific, Massachusetts, USA). Oxide and metal content of each sample was calculated from light microscope images at 125× magnification using greyscale analysis with ImageJ. The average value and standard deviation were determined using five images for each sample. Coating thickness and its standard deviation was determined using the same greyscale images and ImageJ at 10 different locations. The deposition efficiency (DE) was calculated according to DIN EN ISO 17863:2004, which takes the theoretical value of mass delivered to the substrate and the actual mass change of the substrate into consideration. Supplementary, a qualitative XRD phase analysis was performed to identify the formed oxide phases. The measurement was conducted using an X'Pert MPD (Malvern Panalytical Lt., UK) equipped with a copper K_α X-Ray source. Stepping and dwelling were set to 0.0174° and 1.5 s in continuous scan mode. The phase composition of the metallic splats was investigated using SEM imaging and EDS measurements using a FEI Helios NanoLab 600 (FEI Deutschland GmbH, Germany) and Oxford Ultim® Max 40 detector (Oxford Instruments, UK). 8 point-scans were conducted within the metallic phase of each sample. In addition, the overall coating composition was determined using a mapping of the whole Nichrome coating cross-section.

2.3. *Thermal measurements*

The emission coefficient of each sample was determined using a Varioscan 3011 thermal imaging camera (JENOPTIK, Germany) and a reference tape ACLSED (Optris, Germany) with a temperature independent emission coefficient ε of 0.95 as reference. The coefficient was determined in the range of 50 °C and 350 °C in roughly 50 °C steps. Evaluation was carried out with IRBIS professional 2.2 (InfraTec, Germany) adjusting the emission coefficient of the sample area to match the same temperature as the one measured on the reference tape.

Thermal ramping behaviour of the samples was investigated at the University of Stuttgart using an EA PSI 880 DC power supply (EA Elektro-Automatik Inc., USA). The samples were heated at a constant supply voltage of 80 V up to 700 °C. The applied voltage and current were constantly measured directly by integrated sensors in the DC power supply. A maximum measurement error of $U_{\mathrm{error}} < 0.05$ % and $I_{\mathrm{error}} < 0.15$ % is assumed according to the manufacturers data sheet. The heating curves were documented using a CTL-SF75-C3 pyrometer (μ-epsilon, Germany) using the CompactConnect software (Optris, Germany) which has a system accuracy of ±1 % and temperature resolution of 0.1 °C. Note that the resistivity is an average of the entire coating of the heating element, while the related temperature is obtained from the center of the element. Therefore, the measured resistivity values are subject to an indefinite, but small error, since the corners of the element are slightly cooler than the center. However, it does not influence the comparability of the presented data as the elements are identical for all parameters.

Steady state heating experiments have been conducted at University of Modena and Reggio Emilia. A separate set of samples was tested at 700 °C dwelling for 1 h. A 50 Hz AC (Variac power supply) was employed for powering. The applied voltage was gradually increased starting at 20 V until the final voltage was reached to keep the sample constant at 700 °C, resulting in an individual maximum voltage (V_{max}) for each sample. The temperature was recorded using an infrared (IR) thermographic camera (T640, FLIR, USA). The camera has a 30 Hz infrared detector with 640 × 480 resolution, 0.035 °C thermal sensitivity, and −40 to 2000 °C temperature measurement range. Data was acquired at 10 Hz, connecting the camera in real-time to a PC and using FLIR Thermal Studio Suite software. The thermal camera emissivity set point was calibrated by reading the environmental temperature from a reference point on a black surface with emissivity close to 1. Calibration was verified prior to each experimental run. The camera's thermal sensitivity allows for a margin of error within ±0.5 °C within the measured temperature range. Current and voltage were documented using Fluke 323 True RMS Clamp Meter (Fluke Corporation, USA) and a portable multimeter (Metrix MTX3293) every 10 min. The Fluke 323, calibrated bi-annually, offers a ±2 % accuracy in current readings, while the Metrix MTX3293 multimeter, calibrated annually, maintains an accuracy within ±0.5 % for voltage measurements.

2.4. *Data evaluation*

The resistance R_{total} of the complete system was calculated from the obtained voltage V_{total} and electrical current I_{total} values from the experiments. To simplify the calculations as shown in Eq. (1), the contact resistance was assumed to be negligible small as compared to the resistance of the heating element R_{element}, which was verified using a multimeter.

$$R_{element} = V_{total} \bullet I_{total} \tag{1}$$

The specific resistance ρ_{element} was calculated according to Eq. (2).

$$\rho_{element} = R_{element} \bullet \frac{t \bullet w}{l} \tag{2}$$

with w being the meander width, t the coating thickness and l the meander length. Hence, the specific resistivity is suitable to compare the coatings properties independently of their geometric factors, such as for example variations in coating thickness.

3. Results

3.1. *Feedstock materials*

The particle size distribution of the APS powder and the suspension are given in Fig. 2. A PSD of the raw HVOF powder is not added, as it is identical with the one measured for suspension. In addition, the SEM cross-section of the filament is shown to visualize the powder distribution within the filament. The PSD of the suspension corresponds with the values measured for the raw powder. Both exhibit a narrow and monomodal distribution with values of d10 = 3.8 μm and d90 = 12.9 μm. The APS powder has a similar monomodal curve but shifted to higher d10 and d90 values of 6.3 μm and 30.2 μm, respectively. Hence, the distribution coincides with the information stated by the supplier. It can be assumed that no agglomerates are present for the raw powders, and a stable suspension is achieved. In the LM cross section the bright grey spots represent the Ni20Cr particles surrounded by the dark grey polypropylene matrix. Some metal particles at the prepared surface have been removed during the grinding process and are visible as spherical pores with bright corners. Overall, the particles are homogenously distributed within the processed filament.

3.2. *Microstructural analysis*

3.2.1. *Light microscopy*

A high deposition efficiency is achieved for all presented coatings. APS coatings exhibit a deposition efficiency of 62 ± 1 %, while the suspension and filament HVOF coatings exceed that with 77 ± 2 % and 70 ± 3 %. Fig. 3 depicts light microscopy cross-sections of all samples, including the Nichrome coating thickness values. Three layers are visible, on the bottom the steel substrate appearing white, consecutively followed by the Al_2O_3 insulation layer appearing dark grey and the brighter Nichrome coating. In addition, for each sample a close-up image is presented, enlarging the Nichrome coating of the heating element. Within the enlarged image a mottled structure of dark grey and white splats is apparent, of which the white splats represent metallic particles and the darker splats Ni- and Cr-oxides. Upon increasing λ

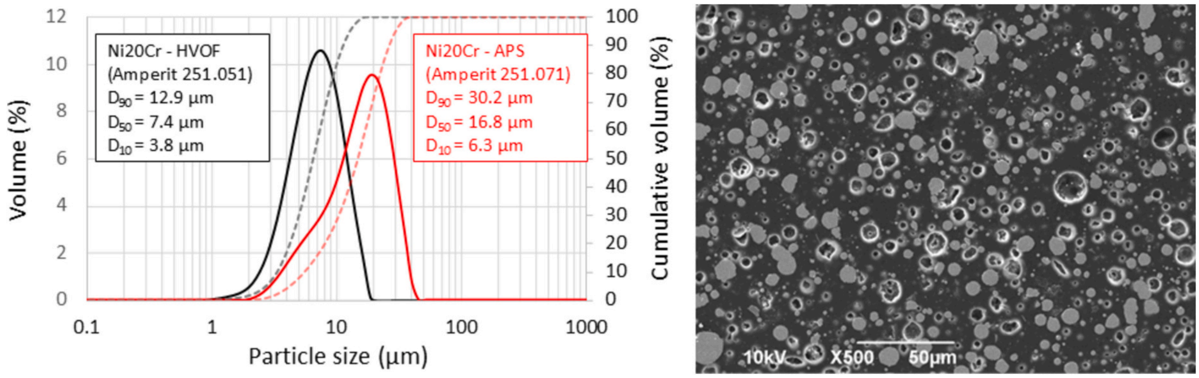

Fig. 2. Left graph: Particle size distribution of Ni20Cr APS powder (red) and Ni20Cr suspension (black). Right image: SEM micrograph of the PP-Ni20Cr filament cross-section, filled with Ni20Cr Amperit 251.051.

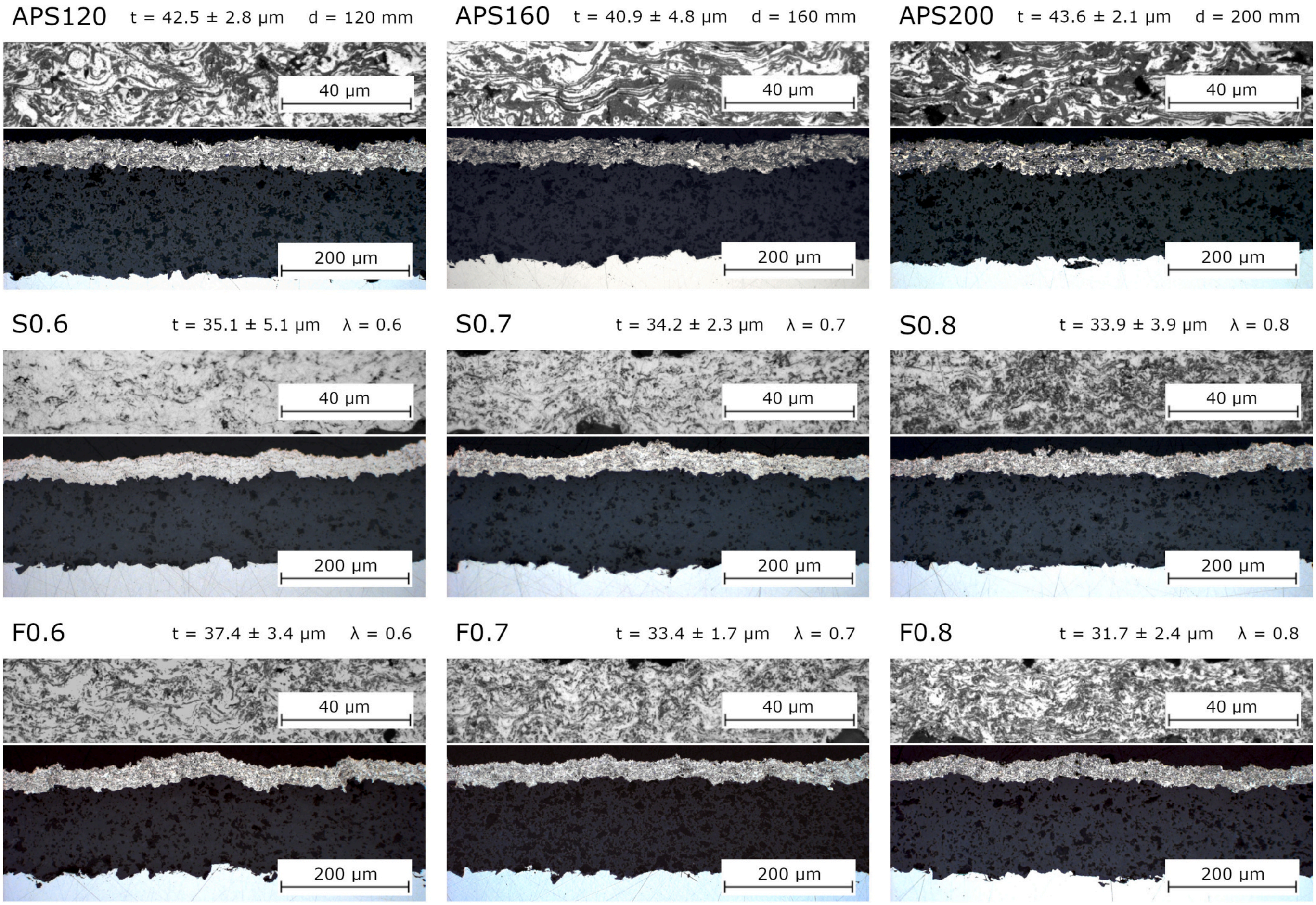

Fig. 3. Light microscopic cross-sections of APS (APS120, APS160 and APS200), suspension (S0.6, S0.7 and S0.8) and filament HVOF (F0.6, F0.7 and F0.8) heating elements. The coating thickness t and varied spraying parameter are listed on top of the images.

(HVOF) or the stand-off distance (APS) the oxide content is increasing within each set of samples.

However, when comparing the processes, APS shows the highest oxide content, suspension based HVOF exhibits the lowest oxidation and filament based HVOF covers the range in between. This visual impression is confirmed by the ImageJ grey scale analysis, which quantifies the oxide content. In Fig. 4 the dependence of oxide content is given as a function *d* and *λ*. The dependency shows a near linear increase of the oxide content with increasing *d* (APS) and increasing *λ* (HVOF). As expected, the pore content for HVOF is low and slightly exceeds 1 vol.-% only for F0.8. For APS the pore content increases significantly with increasing *d*, especially from 160 to 200 mm. All oxide- and porosity-fractions obtained from ImageJ are listed in Table 2. Note that only micropores, but not nanopores, are detected with ImageJ.

3.2.2. *X-ray diffraction analysis (XRD)*

Furthermore, the XRD results in Fig. 5 reveal differences regarding oxide formation. Besides the Ni / Cr (ICSD-064989 / -064712 [36,37]) peaks, NiO (ICSD-064712 [38]), Cr_2O_3 (ICSD-201104 [39]) and $NiCr_2O_4$ (ICDD-064712 [40]) are detected for all APS samples, showing clear

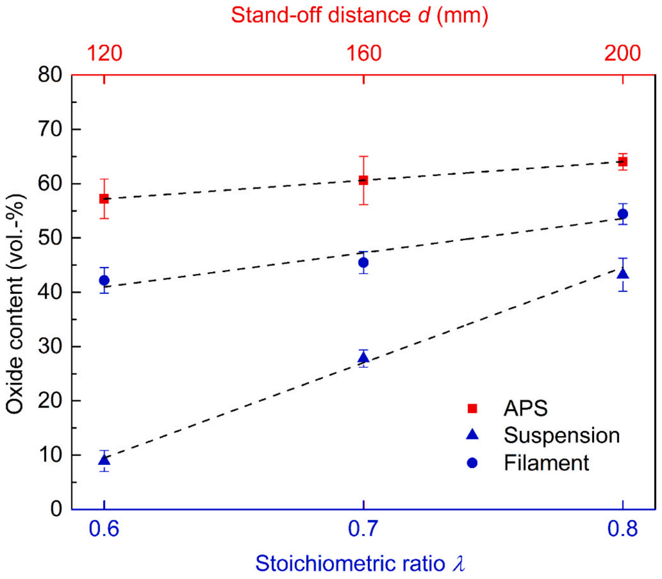

Fig. 4. Oxide content (vol.-%) in dependence of varied spraying parameter stand-off distance d (APS) and stoichiometric ratio λ (HVOF).

peak outlines for every signal. In addition, CrO (ICSD-N.A. [41]) and iron contamination, in form of Fe_3O_4 (ICSD-064712 [42]), is registered for APS120, but not for APS160 and APS200. With increasing standoff distance, the formation of $NiCr_2O_4$ is favored on the cost of Cr_2O_3 and CrO. In the case of suspension and filament HVOF the peaks exhibit a low aspect ratio, meaning a generally broad and shallow appearance. This aspect ratio decreases continuously with decreasing λ. It leads to indistinguishable signals between 34° and 37° 2Θ for all HVOF samples, but especially for the suspension sprayed coatings due to significantly lower oxide content. Nevertheless, NiO, CrO and Cr_2O_3 can be identified for all filament sprayed samples, while for the suspension sprayed samples S0.7 and S0.8 only NiO is recognizable. S0.6 does not show any distinct oxide peaks, due to low oxide content and presumably broad and shallow signals.

3.2.3. *Scanning electron microscopy (SEM) and energy dispersive X-ray analysis (EDS)*

An exemplary SEM image for each sample is given in Fig. 6. The comparatively large particles in APS form a microstructure of either completely oxidized or mostly metallic splats. As a result, large contiguous areas of interconnected metallic paths are formed despite high oxide content. Delamination is only observed in the oxide-metal splat interface. On the contrary, the formed oxide particles in filament and suspension HVOF seem to fragment upon impact and while being incorporated into the metallic matrix do not lead to delamination in the oxide-metal interface. However, delamination occurs in the metal-metal splat interface, especially for low λ and suspension sprayed samples.

EDS mapping of the entire coating cross-section, measuring oxides and the metallic phase, reveals a slightly higher Cr content for APS samples with 20.32 ± 1.08 wt.-% as compared to HVOF samples with 19.03 ± 0.25 wt.-%. The rather large standard deviation of 1.08 wt.-% for APS could be caused due to large splats, resulting in a lower statistical accuracy in the analysis. The point scan analysis reveals a Cr-depletion within the metal phase of the coating, as visualized in Fig. 7, which plots the Cr content of the sample against λ and the stand-off distance d, represented by the solid line. The Cr content decreases linearly with increasing λ or d. This is directly correlated with the oxygen content and, consequently, the oxidation state of the material, as shown by the O wt.-% obtained from the mapping. Consistent with the LM observations in Section 3.2.1, the O content increases with increasing λ or d, being highest for APS, followed by filament HVOF, and lowest for suspension HVOF. The dependency shows a near linear increase in oxygen content with increasing λ (HVOF) and a second-degree polynomial increase with increasing d (APS). Therefore, Cr-depletion can be linked to the oxidation process during thermal spraying. An increase in oxidation results in greater Cr-depletion within the NiCr phase. Oxidation can be almost entirely avoided in suspension HVOF, a Cr content between approximately 18 to 20 wt.-% is maintained. In filament HVOF it ranges from about 14 to 16 wt.-%, while for APS it ranges from approximately 6 to 11 wt.-%. Therefore, for future reference, APS and F0.8 can be categorized as Cr-depleted, while suspension HVOF, F0.6 and F0.7 are considered Cr-rich samples.

3.3. *Heating element characterization (DC source)*

3.3.1. *Emissivity*

The emission coefficients are listed in Table 3. Within each set of samples, ε demonstrates an increasing trend with a rise in oxide content.

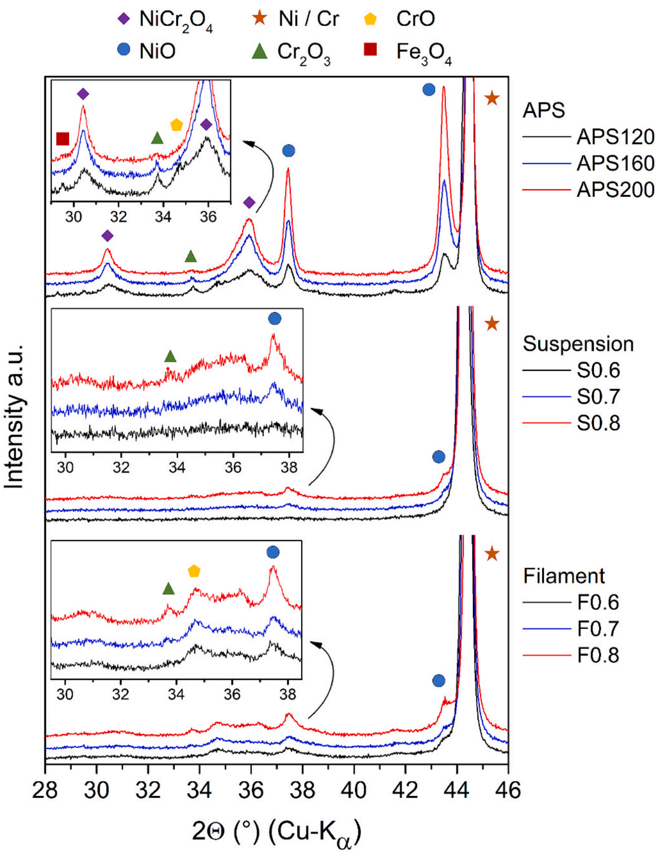

Fig. 5. XRD patterns of the APS and HVOF sprayed Nichrome coatings.

Table 2
Oxide and porosity content of the sprayed Nichrome coatings.

Sample	APS 120	APS 160	APS 200	S0.6	S0.7	S0.8	F0.6	F0.7	F0.8
Oxide [vol.-%]	57.2 ± 3.6	60.6 ± 4.5	64.4 ± 1.5	8.9 ± 1.9	27.8 ± 1.6	43.2 ± 3.1	42.1 ± 2.3	45.5 ± 2.0	54.4 ± 1.9
Porosity [vol.-%]	1.6 ± 1.3	2.7 ± 1.3	4.6 ± 2.4	0.1 ± 0.1	0.5 ± 0.3	0.8 ± 0.2	0.5 ± 0.2	0.3 ± 0.3	1.3 ± 0.6

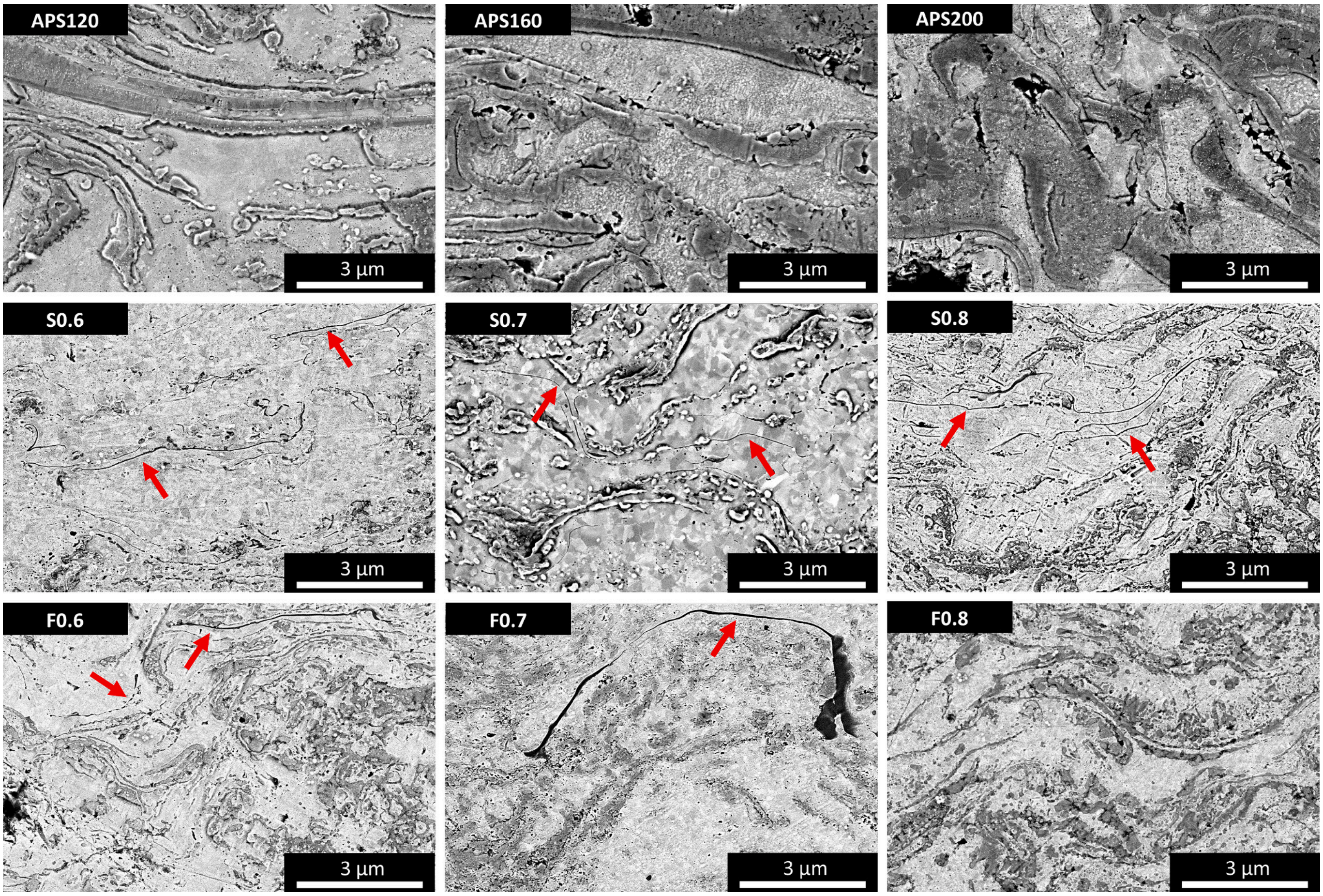

Fig. 6. Electron microscopic cross-sections of APS (APS120, APS160 and APS200), suspension (S0.6, S0.7 and S0.8) and filament HVOF (F0.6, F0.7 and F0.8) heating elements Arrows mark delaminated metal-metal areas.

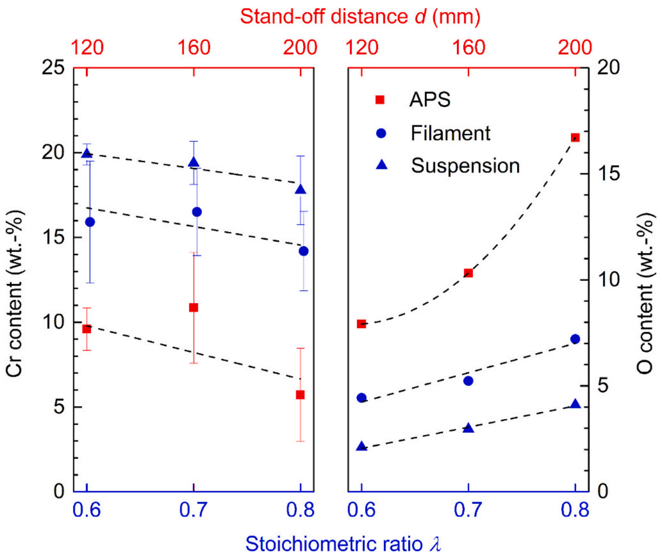

Fig. 7. SEM EDS analysis results. Left side: Cr content of the metallic phase in the coatings. Right side: Oxygen content of the coating cross-section. Both given with respect to λ and d, respectively.

Within each spraying technique an increasing oxide content results in a higher ε. This is also consistent if the filament and suspension sprayed samples are compared. However, the overall oxide content does not manifest consistently across APS and HVOF. For instance, APS120 exhibits a lower ε than all filament HVOF samples despite containing a higher oxide content. It is plausible that this discrepancy is linked to surface conditions, for example surface roughness [43]. Overall, these results align with expectations, given that oxides typically exhibit high emissivity, while metals display higher reflectivity and will not be discussed in detail [44,45].

3.3.2. *Steady state heating*

The steady state temperature curve, one hour at 700 °C, is given in Fig. 8. All samples show a stable temperature profile with small temperature fluctuations of maximum ±5 °C. During the testing period the conductivity of the sample was tracked. No significant changes were observed. Therefore, the fluctuations can be attributed to external factors, such as changes in the surrounding atmosphere e.g. changes in convective heat transfer due to varying air flow.

3.3.3. *Thermal ramping behaviour*

The thermal ramping curves tested at U = 80 V DC are presented in Fig. 9. The curve can be sectioned into two domains. First, the low temperature domain from RT to 400 °C with a near linear heating behaviour for all samples. Hence, Fig. 9 focuses on the second, high temperature domain above 400 °C, in which differences in heating behaviour become more prominent. In this domain all Cr-depleted samples heating rates noticeably decrease and causes the curve to converge towards a maximum temperature limit $T_{\max}$. However, except for APS200 ($T_{\max}$ = 623 °C) the maximum temperature is not fully reached at 700 °C. In case of the Cr-rich samples the low temperature domain is followed by a transitional regime with an initial, less pronounced decline in heating rate before reaching a constant, near linear

Table 3
List of emission coefficients for the sprayed APS and HVOF in the temperature range of RT - 350 °C.

Sample	APS 120	APS 160	APS 200	S0.6	S0.7	S0.8	F0.6	F0.7	F0.8
ε	0.818 ± 0.008	0.822 ± 0.005	0.841 ± 0.009	0.784 ± 0.006	0.814 ± 0.005	0.828 ± 0.011	0.832 ± 0.012	0.836 ± 0.004	0.842 ± 0.005

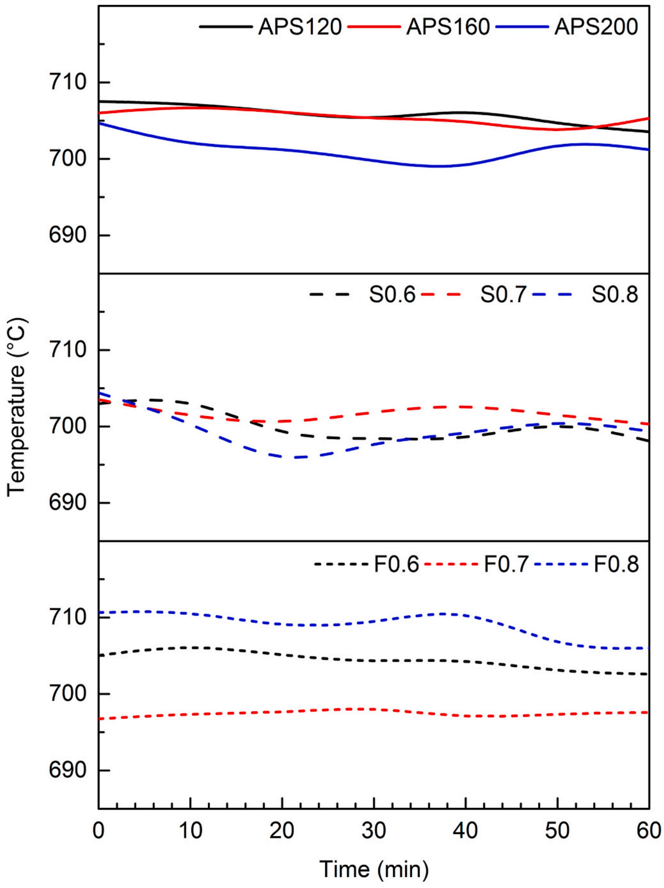

Fig. 8. Steady state heating curves at 700 °C for one hour. Top: Plasma sprayed samples. Middle: Suspension sprayed HVOF. Bottom: Filament sprayed HVOF.

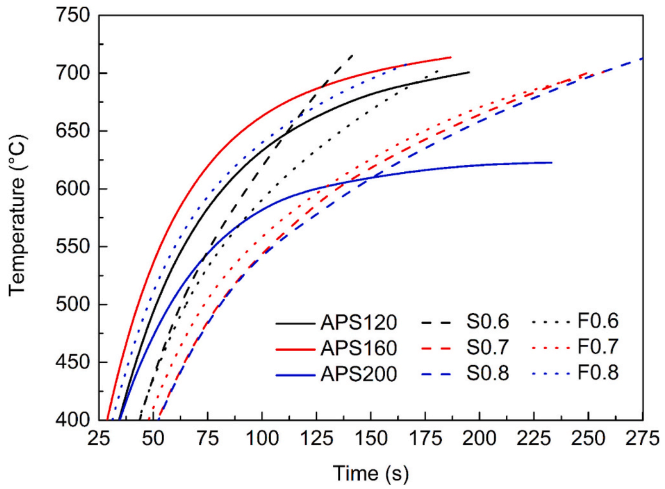

Fig. 9. Heating curves up to 700 °C at U = 80 V DC.

heating behaviour. Specifically, samples sprayed at low λ pertain a high heating rate up to 700 °C, e.g. S0.6 and F0.6. The differences are directly correlated to the temperature dependence of resistivity, since the heating is proportional to the current flow through the sample at constant voltage. In order to attain a better understanding the resistivity data is presented in the next chapter.

3.3.4. Resistivity measurements

Table 4 shows the values of resistance and specific resistivity ρ_0 (correlated to RT) for all heating elements. The resistivity ρ_0 does not show a straightforward correlation to the spraying parameters. In example, a lower λ or a shorter stand-off distance, resulting in lower oxidation, does not necessarily lead to a lower resistivity and vice versa. However, the higher oxidized and therefore Cr-depleted APS samples demonstrate the lowest resistivity values ρ_0 of 0.94 to 1.63 $\Omega\text{mm}^2/\text{m}$. Followed by filament HVOF with 1.19 to 2.24 $\Omega\text{mm}^2/\text{m}$ and last suspension HVOF with 2.40 to 2.69 $\Omega\text{mm}^2/\text{m}$. The errors given in Table 4 are calculated based on error propagation using Eqs. (1) and (2) with the given accuracy of the power supply (see chapter 2.3). Note that the rather high error of ρ_0 for the suspension sprayed samples and F0.6 are dominated by the contribution of coating thickness deviation (see Fig. 3).

The temperature dependency of the normed resistivity ρ/ρ_0 is shown in Fig. 10. A higher temperature dependency can generally be correlated to a higher stand-off distance and higher λ. Opposing the low initial resistivity ρ_0, the temperature dependence is highest for APS, followed by filament HVOF and is least for suspension HVOF. As described, the low temperature domain up to 400 °C all samples show a near linear increase during heating. Due to large differences of ρ_0 the heating curve up to 400 °C is dominated by ρ_0. At higher temperatures ρ increases continuously for the Cr-depleted samples up to at least twice ρ_0. The Cr-rich samples show a decline in ρ at a sample specific critical temperature T_{crit}, which correlates to the transitional regime observed in the heating curves. Similar to the observed temperature dependence of resistivity, T_{crit} displays a tendency to decrease with λ. The only exceptions are S0.7 and S0.6, which display similar values in T_{crit}. As consequence of low temperature dependence and T_{crit}, S0.6 and S0.7 exhibit a lower resistivity at 700 °C than ρ_0, resulting in $\rho/\rho_0 < 1$.

4. Discussion

Although no direct correlation between oxide content and resistance of the samples can be inferred, various factors can be associated with the measured resistance values, providing explanations for the performance differences observed among samples. Besides oxidation, splat interfaces, pore content, phase composition of the metallic phase, internal stresses and defect density, all play a crucial role for the electrical conductivity and its temperature dependence. A detailed analysis of all influences reaches beyond the scope of this study. However, the presumably most important factors, namely oxidation, phase composition of the metallic phase and microstructure are assessed.

4.1. Oxide formation

In general, APS subjects particles to extremely high temperatures and relatively low particle velocities, usually reaching particle temperatures of up to 4250 °C and particle velocities of 100 to 400 m/s [46]. Consequently, pronounced oxidation occurs (see Fig. 4), as oxidization is thermally activated, leading to the formation of equilibrium oxide

Table 4
Resistance and specific resistivity ρ_0 (at RT) of the heating elements.

Sample	APS 120	APS 160	APS 200	S0.6	S0.7	S0.8	F0.6	F0.7	F0.8
R [Ω]	4.21 ± 0.008	2.51 ± 0.005	3.45 ± 0.007	7.51 ± 0.015	8.63 ± 0.017	8.22 ± 0.016	6.57 ± 0.013	6.95 ± 0.014	4.12 ± 0.008
ρ_0 [$\Omega mm^2/m$]	1.63 ± 0.11	0.94 ± 0.11	1.37 ± 0.07	2.40 ± 0.35	2.69 ± 0.18	2.54 ± 0.30	2.24 ± 0.21	2.11 ± 0.11	1.19 ± 0.09

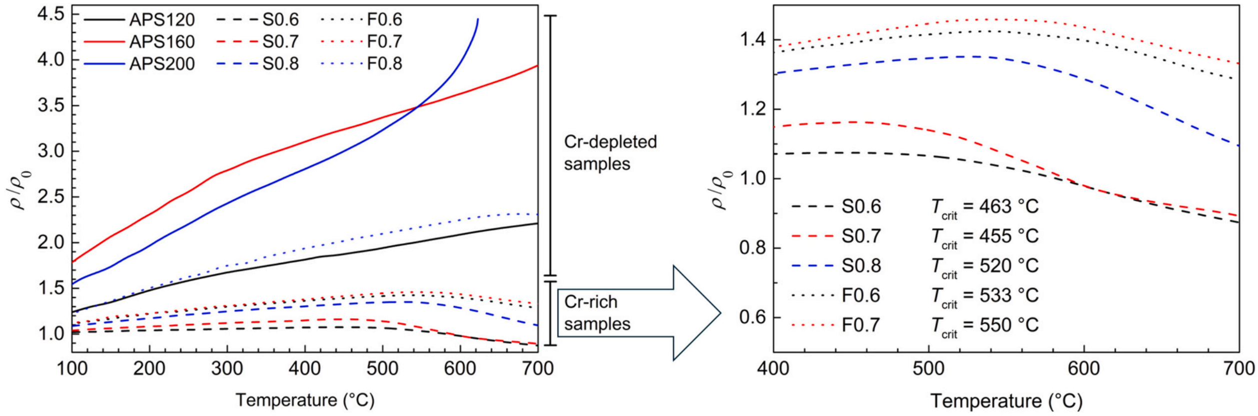

Fig. 10. Normed specific resistivity ρ/ρ_0 between 100 °C and 700 °C (right image) and a selected enlarged area between 400 °C and 700 °C (right image) including T_{crit}.

phases with distinct peaks (see Fig. 5). The observed increase in oxide content with an increment in the stand-off distance d can be attributed to an extended time-in-flight of the metallic particles, resulting in pronounced oxidation and consecutively increased formation of $NiCr_2O_4$. The disappearance of Fe_3O_4 for APS160 and APS200 might be linked to the formation of $NiFe_2O_4$, which would overlap with the $NiCr_2O_4$ signal [47]. In contrast, the HVOF-based processes exhibit significantly lower flame and particle temperatures and reduced time-in-flight, owing to high particle velocities. Maximum particle temperatures of roughly 2700 °C and common particle velocities of >1000 m/s have been reported for water-based suspension spraying with HVOF by Trache [48]. Coupled with an oxygen deficiency in the sub-stoichiometric flame, it contributes to a diminished formation of oxides [21,49,50]. The oxygen deficiency within the flame also induces peak broadening, as it is likely that various sub-stoichiometric oxides and possibly transient oxides are formed [51–53]. It coincides with oxide quantification conducted as the visual ImageJ analysis reveals a rather high oxide content for the HVOF samples when compared to the measured oxygen wt.-% in the EDS analysis. The disparity in amount of oxide formation and peak shape between suspension and filament based HVOF is mainly caused by the dispersing media used for spraying. Water takes up a substantial amount of energy due to its high vaporization enthalpy, whereas the polymer matrix adds a minor amount of combustion enthalpy to the flame [54,55]. Therefore, in the case of filament-based HVOF, a small amount of additional energy is introduced into the flame, whereas, in water-based suspension HVOF, thermal energy is withdrawn. Additionally, the droplet formation in suspension HVOF may shield metallic particles from oxidation until the water is vaporized, leading to a shorter effective exposure to heat and oxygen [18]. Overall, it an increase in oxide formation reduces the effective conductive cross section of the coating and therefore negatively affects the conductivity of the coating. Nevertheless, many factors beyond the total amount of oxide significantly influence how oxides affect conductivity. These include the oxide type, its location and its stoichiometry. For instance, oxide may form along grain boundaries, within individual splats, or as fully oxidized splats, each having a distinct impact on conductivity [56–58]. Furthermore, at high temperatures, certain oxides behave as weak conductors rather than insulators, especially when sub-stoichiometric. Since it is not possible to isolate these different factors in the coatings studied, it cannot be quantified to which extend the total oxide content affects conductivity. Moreover, oxidation is intertwined with phase composition changes of the Ni20Cr alloy of the powder and is discussed in the next section.

4.2. Metallic phase composition

The overall Cr content of the coating obtained from EDS mapping, including both oxide and metal phases, matches the values specified in the producer's certificate of analysis. However, the oxidation of Ni20Cr during thermal spraying results in an alteration of the Ni:Cr ratio within the conductive phase due to preferred oxidation of Cr. Even though it is not apparent from the chromium oxide peaks within the XRD results, EDS point scans reveal a depletion of Cr within the metallic phase. Generally, Nichrome alloys resistivity decreases with decreasing Cr content. In example, resulting in a roughly two times lower resistivity at room temperature for 10 wt.-% as compared to 20 wt.-% Cr. [32,59] Hence, resistivity at room temperature of the conductive phase within the coatings increases with decreasing oxidation. With respect to the sprayed coatings, the resistivity of the metallic phase should increase from suspension to filament HVOF to APS. Analogous, Cr-rich Nickel alloys exhibit a slightly lower temperature dependence of ρ [32,60], resulting in a stronger increase of ρ with increased oxidation of the coating. Even though the general tendency of ρ_0 and temperature dependence of ρ (see Table 4 and Fig. 10) reflects the expected behaviour, within each set of samples of the different spraying techniques minor irregularities occur. Furthermore, the atypical reduction of resistivity at T_{crit} for the suspension and filament sprayed coatings cannot be explained using the presented chain of arguments. Consequently, these have to be a result of microstructural features such as splat-splat interfaces.

4.3. Microstructure analysis

From the SEM images three major influence factors on the coating resistivity can be identified. First, the number of splat-splat boundaries is far higher for HVOF due to smaller primary particles. However, splat-splat boundaries are difficult to quantify in terms of their influence on the resistivity as it is a function of splat size (splat boundary density), degree of splat flattening, micro- and nano porosity, oxide skin formation and possibly metallurgical inter-splat connections [56–58,61–66]. Conceivably, the significant increase of splat boundary density due to small particle size in HVOF contributes significantly to a higher resistivity, which is likely to be the major cause for the predominantly higher resistivity observed for HVOF compared to APS. Sharma et al. showed that an increase in splat boundary density within the current direction can lead to a significant decrease in electrical conductivity for APS [56]. In addition, the large metallic splats in APS sprayed coatings offer a rather direct conductive path along the splats. In contrast, the seemingly fragmented oxides in HVOF may disturb a direct conductive path, prolonging the overall effective path length through the coating. Second, the observed metal-metal splat delamination within the HVOF samples increases the resistivity of the coating by decreasing the effective conductive cross section. From the SEM images delamination in HVOF shows the tendency to occur more frequent with decreasing λ. It is possible that the fragmentation of oxides leads to a dispersive phase that prevents the build-up of high internal stresses. Thus, an increase in oxidation leads to less delamination between metal-metal splats [67,68]. At the same time, the fragments are small enough to not delaminate either. Contrary, APS splats solely delaminate in the metal-oxide interface having no effect on the conductivity of the coating. The metal-oxide delamination is likely caused by high interface stresses due to the large splat size. Third, the porosity increases significantly for APS coatings with increasing stand-off distance, negatively effecting the conductivity and likely being the reason for APS200 having a higher resistivity ρ_0 than APS160 [69,70]. Further, the significant increase in defects such as pores alongside the high oxide content may be the reason an abnormal increase of ρ for APS200 approaching 600 °C. For HVOF no relevant changes in porosity are observed for the presented parameter set.

4.4. *Temperature dependence of resistivity and heating performance*

Taking all previously discussed factors into account the resistivity curve and therefore the correlating heating performance of the low and high temperature domain, as well as the transition region for Cr-rich coatings, can be explained. The heating performance within the low temperature regime is dominated by the initial resistivity ρ_0. Therefore, the highly oxidized and thus Cr-depleted samples, despite having a higher temperature dependence of ρ, heat up faster (see Fig. 9). However, in the high temperature domain above 400 °C the temperature dependence becomes a dominating factor. It leads to a notably decline in heating rate as heat generation decreases and heat transfer to the surrounding increases. Consequently, Cr-depleted samples converge towards a maximum temperature. APS200 is reaching $T_{\max}$ at 623 °C, while it is not yet fully reached for APS120, APS160 and F0.8 at 700 °C. Contrary, the Cr-rich samples do not converge due to a rather low temperature dependent increase of ρ up to T_{crit}, followed by a decrease in the high temperature regime ($T > T_{\text{crit}}$). The irregular decline in resistivity for these samples is likely correlated to the delamination between metal-metal splats, as previously discussed. When heating up the splats expand closing the delaminated areas. Therefore, the conductivity increases at elevated temperatures, leading to a near linear heating curve. In long term application the Cr-rich coating properties should permanently converge to lower ρ due diffusion processes taking place. In addition, the resistivity should display a low temperature dependence with a linear progression similar to the reported results by Prudenziati et al. [30]. However, avoiding splat delamination entirely by adjusting the spraying process would be preferable.

4.5. *Process classification and comparative analysis*

As noted in the introduction, there is significant interest in the energy sector for electrical heating applications, such as reactors used in hydrogen production. Producing hydrogen requires temperatures around 800 °C. For Nichrome coatings to remain stable at these high temperatures, it is essential to maintain a Cr content above 15 wt.-%, which facilitates the formation of a dense, protective Cr_2O_3 layer [52,71–74]. Without this layer, the coating will experience full oxidation over time, compromising long-term stability. According to the findings of this investigation and the presented reference data, techniques like APS and suspension HVOF allow for precise adjustment of the oxidation levels, thereby enabling control over the Cr content in the metallic phase of the coating relative to the original powder composition. However, this degree of oxidation control is not achievable with filament HVOF. To attain the desired Cr content with filament HVOF, excess chromium in the raw powder can compensate for oxidation loss, or conventional powder-based HVOF may be used if thicker coatings are acceptable. Each coating technique varies in terms of processability. Conventional powder-based HVOF and APS are generally limited to coating thicknesses above 30 μm, beyond which the coating's structural integrity may be compromised, leading to higher failure rates under high loads and high scrap rates in production. In contrast, both suspension and filament HVOF allow for much thinner coatings, starting at just a few microns, which enhances structural versatility in applications. From a production cost perspective, thinner coatings are preferable as they reduce processing times, comprising coating fabrication and subsequent laser structuring. Filament HVOF offers simplicity and accessibility for mass production, whereas suspension HVOF is more technically demanding and requires specialized equipment and maintenance, limiting its scalability. Overall, these techniques all support high-temperature applications when the coating parameters are tailored appropriately. The systematic investigation presented in the paper allows selecting a suitable method and optimizing parameters to fine-tune the desired coating properties, which is an essential factor for effective resistant heaters [75].

5. Conclusion

Nichrome coatings were produced by three different coating techniques, APS, filament and suspension HVOF. The effects of spraying parameters and spraying technique on the microstructure (Section 3.2) and heating performance (Section 3.3) were explored. Differences in the oxide content, oxidation behaviour and Cr-depletion were determined by image analysis, XRD and EDS. This study allows drawing the following conclusions:

- The oxide content of the coatings can be adjusted across a broad range (8.9 to 64.4 vol.-%), resulting in varying heating behaviors. Plasma-sprayed coatings exhibit the highest oxide content (57.2 to 64.4 vol.-%), followed by filament-based HVOF coatings (42.1 to 54.4 vol.-%). Suspension-based HVOF coatings show the lowest oxidation levels (8.9 to 43.2 vol.-%). Significant oxidation in APS coatings leads to distinct oxide peak formation in XRD (Cr_2O_3, $NiCr_2O_4$, and NiO), whereas in HVOF coatings, primarily non-equilibrium oxides are formed, even at higher oxide fractions, as confirmed by the oxygen content in EDS analysis.
- Increasing oxidation results in greater Cr-depletion, as Cr is preferentially oxidized. The Cr content in the metallic phase varies between 6 and 11 wt.-% for APS coatings, around 14 to 16 wt.-% for filament-based HVOF coatings, and 18 to 20 wt.-% for suspension-based HVOF coatings. Despite the increase in oxidation at $\lambda = 0.7$ and 0.8, suspension HVOF shows minimal changes in its Ni ratio due to the low oxygen content within the oxide phases. Therefore, water-based suspensions effectively reduce oxidation of the metallic powder.
- Filament and suspension HVOF techniques enable the spraying of finely structured, homogeneous Nichrome coatings with low porosity due to the small primary particle size of the sprayed powder. In contrast, APS is limited to coatings above ~40 μm due to coarser microstructure and higher porosity. However, HVOF-based methods tend to be more susceptible to inter-splat delamination within the

metallic phase, whereas APS primarily experiences delamination at the oxide-metal interface.

- The electrical properties of the Nichrome coatings, specifically temperature dependence and ρ_0, are primarily influenced by the Cr content in the metallic phase rather than the oxide fraction. Increased oxidation significantly reduces the ρ_0, but it also leads to a notable increase in temperature dependence.
- Among the techniques, suspension HVOF coatings proved to be the most versatile for resistant heater applications. Their widely adjustable oxide content and minimal changes in material composition (Ni:Cr ratio) at low λ provide a clear advantage over APS and filament HVOF coatings, which undergo more significant material transformations.

CRediT authorship contribution statement

Marvin Sauter: Writing – original draft, Visualization, Validation, Methodology, Investigation, Formal analysis, Data curation, Conceptualization. **Christian Semmler:** Writing – review & editing, Writing – original draft, Validation, Methodology, Conceptualization. **Tobias Nies:** Validation, Investigation, Formal analysis, Data curation. **Giulia Poppi:** Writing – original draft, Validation, Investigation, Data curation. **Luca Bortolotti:** Validation, Investigation, Data curation, Writing – review & editing. **Filippo Ottani:** Validation, Investigation. **Giovanni Bolelli:** Writing – review & editing, Validation, Resources, Project administration, Investigation. **Luca Lusvarghi:** Writing – review & editing, Resources, Project administration. **Andreas Killinger:** Resources, Project administration, Writing – review & editing.

Declaration of Generative AI and AI-assisted technologies in the writing process

During the preparation of this work the authors used ChatGPT in order to improve language and readability. After using this tool, the authors reviewed and edited the content as needed and take full responsibility for the content of the publication.

Funding

This research did not receive any specific grant from funding agencies in the public, commercial, or not-for-profit sectors.

Declaration of competing interest

The authors declare that they have no known competing financial interests or personal relationships that could have appeared to influence the work reported in this paper.

Acknowledgements

The authors would like to express their gratitude to Dr.-Ing. Michael Beltle from the IEH Universität Stuttgart for providing the AC power source needed to conduct the presented experiments.

Appendix A. Supplementary data

Supplementary data to this article can be found online at https://doi.org/10.1016/j.surfcoat.2024.131594.

Data availability

Data will be made available on request.

References

[1] Ipcc, Global Warming of 1.5°C: IPCC Special Report on Impacts of Global Warming of 1.5°C above Pre-industrial Levels in Context of Strengthening Response to Climate Change, Sustainable Development, and Efforts to Eradicate Poverty, 1st ed., Cambridge University Press, 2022 https://doi.org/10.1017/9781009157940.

[2] Wiley-VCH (Ed.), Ullmann's Encyclopedia of Industrial Chemistry, 1st ed., Wiley, 2003 https://doi.org/10.1002/14356007.

[3] J. Matthies, T. Schall, W. Pritzkow, U. Tuttlies, U. Nieken, Electrically heated oxide ceramic tubes for high temperature reactions, Chem. Ing. Tech. 95 (2023) 701–707, https://doi.org/10.1002/cite.202200186.

[4] G. Kolious, Gasdichtes, wärmedurchlässiges, keramisches und mehrlagiges Verbundrohr, EP 3 835 639 A1, 2021.

[5] T. Sundararaian, S. Kuroda, T. Itagaki, F. Abe, in: B.R. Marple, C. Moreau (Eds.), Steam Oxidation Resistance of HVOF Thermal Sprayed Ni-Cr Coatings, 2003, pp. 495–502, https://doi.org/10.31399/asm.cp.itsc2003p0495. Orlando, Florida, USA.

[6] N. Bala, H. Singh, S. Prakash, Accelerated hot corrosion studies of cold spray Ni–50Cr coating on boiler steels, Mater. Design 31 (2010) 244–253, https://doi.org/10.1016/j.matdes.2009.06.033.

[7] K. Yamada, Y. Tomono, J. Morimoto, Y. Sasaki, A. Ohmori, Hot corrosion behavior of boiler tube materials in refuse incineration environment, Vacuum 65 (2002) 533–540, https://doi.org/10.1016/S0042-207X(01)00468-7.

[8] T.S. Sidhu, S. Prakash, R.D. Agrawal, Hot corrosion studies of HVOF sprayed Cr3C2–NiCr and Ni–20Cr coatings on nickel-based superalloy at 900 °C, Surf. Coat. Technol. 201 (2006) 792–800, https://doi.org/10.1016/j.surfcoat.2005.12.030.

[9] B.S. Sidhu, S. Prakash, Performance of NiCrAlY, Ni–Cr, Stellite-6 and Ni3Al coatings in Na2SO4–60% V2O5 environment at 900 °C under cyclic conditions, Surf. Coat. Technol. 201 (2006) 1643–1654, https://doi.org/10.1016/j.surfcoat.2006.02.035.

[10] D. Tejero-Martin, M. Rezvani Rad, A. McDonald, T. Hussain, Beyond traditional coatings: a review on thermal-sprayed functional and smart coatings, J. Therm. Spray Tech. 28 (2019) 598–644, https://doi.org/10.1007/s11666-019-00857-1.

[11] K. Bobzin, M. Öte, M.A. Knoch, I. Alkhasli, Temperature distribution on thermally sprayed heating conductor coatings, IOP Conf. Ser. Mater. Sci. Eng. 480 (2019) 012002, https://doi.org/10.1088/1757-899X/480/1/012002.

[12] S.T. Dehaghani, A. Dolatabadi, A. McDonald, Thermally sprayed metal matrix composite coatings as heating systems, Appl. Therm. Eng. 196 (2021) 117321, https://doi.org/10.1016/j.applthermaleng.2021.117321.

[13] K. Bobzin, W. Wietheger, M.A. Knoch, A. Schacht, Heating behaviour of plasma sprayed TiOx/Cr2O3 coatings for injection moulding, Surf. Coat. Technol. 399 (2020) 126199, https://doi.org/10.1016/j.surfcoat.2020.126199.

[14] M. Floristán, R. Fontarnau, A. Killinger, R. Gadow, Development of electrically conductive plasma sprayed coatings on glass ceramic substrates, Surf. Coat. Technol. 205 (2010) 1021–1028, https://doi.org/10.1016/j.surfcoat.2010.05.033.

[15] M. Gardon, J.M. Guilemany, Milestones in functional titanium dioxide thermal spray coatings: a review, J. Therm. Spray Technol 23 (2014) 577–595, https://doi.org/10.1007/s11666-014-0066-5.

[16] R.C. Tucker (Ed.), ASM handbook. 5A: Thermal spray technology / vol. ed. Robert C. Tucker, ASM International, Materials Park, Ohio, 2013.

[17] L. Pawłowski, The Science and Engineering of Thermal Spray Coatings, 2nd ed, Wiley, Chichester, England, Hoboken, NJ, 2008.

[18] P. Fauchais, J. Heberlein, M. Boulos, Thermal Spray Fundamentals: From Powder to Part, 2013, https://doi.org/10.1007/978-0-387-68991-3.

[19] M. Hauer, B. Ripsch, A. Gericke, W. Krömmer, K.-M. Henkel, Advanced analyses of heating elements manufactured by an optimized arc spraying process, Coatings 13 (2023) 1701, https://doi.org/10.3390/coatings13101701.

[20] A. Killinger, R. Gadow, Thermally Sprayed Coating Composites for Film Heating Devices, 2006, pp. 1230–1239, https://doi.org/10.4028/www.scientific.net/AST.45.1230.

[21] Krieg Blum, Gadow Killinger, Trenkle Luth, High velocity suspension flame spraying (HVSFS) of metal suspensions, Materials 13 (2020) 621, https://doi.org/10.3390/ma13030621.

[22] M. Sauter, A. Roth, A. Grebhardt, A. Killinger, High velocity flame spraying of highly-filled ceramic — polymer filaments (F-HVOF), Surf. Coat. Technol. 458 (2023) 129324, https://doi.org/10.1016/j.surfcoat.2023.129324.

[23] L. Pawlowski, Suspension and solution thermal spray coatings, Surf. Coat. Technol. 203 (2009) 2807–2829, https://doi.org/10.1016/j.surfcoat.2009.03.005.

[24] R. Rampon, O. Marchand, C. Filiatre, G. Bertrand, Influence of suspension characteristics on coatings microstructure obtained by suspension plasma spraying, Surf. Coat. Technol. 202 (2008) 4337–4342, https://doi.org/10.1016/j.surfcoat.2008.04.006.

[25] F.-L. Toma, A. Potthoff, L.-M. Berger, C. Leyens, Demands, potentials, and economic aspects of thermal spraying with suspensions: a critical review, J. Therm. Spray Technol. 24 (2015) 1143–1152, https://doi.org/10.1007/s11666-015-0274-7.

[26] M. Aghasibeig, F. Tarasi, R.S. Lima, A. Dolatabadi, C. Moreau, A review on suspension thermal spray patented technology evolution, J. Therm. Spray Technol. 28 (2019) 1579–1605, https://doi.org/10.1007/s11666-019-00904-x.

[27] M. Prudenziati, Development and the implementation of high-temperature reliable heaters in plasma spray technology, J. Therm. Spray Technol. 17 (2008) 234–243, https://doi.org/10.1007/s11666-008-9164-6.

[28] D. Michels, J. Hadeler, J.H. Lienhard V, High-heat-flux resistance heaters from vps and hvof thermal spraying, Exp. Heat Transfer 11 (1998) 341–359, https://doi.org/10.1080/08916159808946570.

[29] I.G.C. Dryden, The efficient use of energy, in: Butterworth Scientific in Collaboration with the Institute of Energy Acting on Behalf of the UK Dept. of Energy, London, 2nd ed, 1982.

[30] M. Prudenziati, M.L. Gualtieri, Electrical properties of thermally sprayed Ni- and Ni20Cr-based resistors, J. Therm. Spray Technol. 17 (2008) 385–394, https://doi.org/10.1007/s11666-008-9187-z.

[31] A. Marucco, B. Nath, Effects of ordering on the properties of Ni-Cr alloys, J. Mater. Sci. 23 (1988) 2107–2114, https://doi.org/10.1007/BF01115776.

[32] A.A. Al-Aql, Electrical resistivity measurements in Ni–Cr alloys, Mater. Des. 24 (2003) 547–550, https://doi.org/10.1016/S0261-3069(03)00093-1.

[33] H. Kummer, M. Winkelmann, F. Wüst, S. Hartmann, F. Trenkle, P. Krieg, A. Killinger, Suspension Sprayed Thin Metallic Coatings for Electric Panel Heaters, in: Vienna, Austria, 2022, pp. 581–585, https://doi.org/10.31399/asm.cp.itsc2022p0581.

[34] F. Trenkle, M. Winkelmann, F. Wüst, J. Luth, S. Hartmann, P. Krieg, A. Killinger, Dünne metallische Heizschichten, hergestellt durch Suspensionsspritzen, Therm. Spray Bull. 12 (2019) 72–76.

[35] M. Prudenziati, G. Cirri, P.D. Bo, Novel high-temperature reliable heaters in plasma spray technology, J. Therm. Spray Technol. 15 (2006) 329–331, https://doi.org/10.1361/105996306X124293.

[36] H.E. Swanson, G.M. Ugrinic, Circular of the Bureau of Standards no. 539 Volume 5: Standard x-ray Diffraction Powder Patterns, National Bureau of Standards, Gaithersburg, MD, 1955, https://doi.org/10.6028/NBS.CIRC.539v5.

[37] M.E. Straumanis, C.C. Weng, The precise lattice constant and the expansion coefficient of chromium between +10 and +60° C, Acta Crystallogr. 8 (1955) 367–371, https://doi.org/10.1107/S0365110X55001254.

[38] R.W. Cairns, E. Ott, X-ray studies of the system nickel—oxygen—water. I. Nickelous oxide and hydroxide [1], J. Am. Chem. Soc. 55 (1933) 527–533, https://doi.org/10.1021/ja01329a013.

[39] L.W. Finger, R.M. Hazen, Crystal structure and isothermal compression of Fe2O3, Cr2O3, and V2O3 to 50 kbars, J. Appl. Phys. 51 (1980) 5362–5367, https://doi.org/10.1063/1.327451.

[40] O. Crottaz, F. Kubel, H. Schmid, Jumping crystals of the spinels NiCr2O4 and CuCr2O4, J. Mater. Chem. 7 (1997) 143–146, https://doi.org/10.1039/a604758k.

[41] H. Lux, E. Proeschel, Über das Chrom(II)-oxyd, Z. Anorg. Chem. 257 (1948) 73–78, https://doi.org/10.1002/zaac.19482570107.

[42] V.L. Mazzocchi, C.B.R. Parente, Refinement of the ferri- and paramagnetic phases of magnetite from neutron multiple diffraction data, J. Appl. Cryst. 31 (1998) 718–725, https://doi.org/10.1107/S0021889898004324.

[43] H. Jo, J.L. King, K. Blomstrand, K. Sridharan, Spectral emissivity of oxidized and roughened metal surfaces, Int. J. Heat Mass Transf. 115 (2017) 1065–1071, https://doi.org/10.1016/j.ijheatmasstransfer.2017.08.103.

[44] I. Setién-Fernández, T. Echániz, L. González-Fernández, R.B. Pérez-Sáez, M. J. Tello, Spectral emissivity of copper and nickel in the mid-infrared range between 250 and 900°C, Int. J. Heat Mass Transfer 71 (2014) 549–554, https://doi.org/10.1016/j.ijheatmasstransfer.2013.12.063.

[45] I. González De Arrieta, T. Echániz, J.M. Olmos, R. Fuente, I. Urcelay-Olabarría, J. M. Igartua, M.J. Tello, G.A. López, Evolution of the infrared emissivity of Ni during thermal oxidation until oxide layer opacity, Infrared Phys. Technol. 97 (2019) 270–276, https://doi.org/10.1016/j.infrared.2019.01.002.

[46] K.R. Yu, C.V. Cojocaru, F. Ilinca, E. Irissou, Ensemble methods for APS in-flight particle temperature and velocity prediction considering torch electrodes ageing, J. Therm. Spray Technol. 32 (2023) 175–187, https://doi.org/10.1007/s11666-022-01472-3.

[47] S. Musić, D. Balzar, S. Popović, M. Gotić, I. Czak, S. Dalipi, Formation and Characterization of NiFe204, (n.d.).

[48] R. Trache, Thermisches Spritzen mit wasserbasierten Suspensionen - Von der Injektion zur Schicht, Technische Universität Dresden. https://nbn-resolving.org/urn:nbn:de:bsz:14-qucosa-234350, 2018. (Accessed 15 October 2021).

[49] H. Ruiz-Luna, D. Lozano-Mandujano, J.M. Alvarado-Orozco, A. Valarezo, C. A. Poblano-Salas, L.G. Trápaga-Martínez, F.J. Espinoza-Beltrán, J. Muñoz-Saldaña, Effect of HVOF processing parameters on the properties of NiCoCrAlY coatings by design of experiments, J. Therm. Spray Technol. 23 (2014) 950–961, https://doi.org/10.1007/s11666-014-0121-2.

[50] M. Blum, E. Gyoktepeliler-Akin, A. Killinger, High velocity suspension flame spraying of AlN/Al2O3 composite coatings, Surf. Coat. Technol. 441 (2022) 128588, https://doi.org/10.1016/j.surfcoat.2022.128588.

[51] B. Song, M. Bai, K.T. Voisey, T. Hussain, Role of oxides and porosity on high-temperature oxidation of liquid-fueled HVOF thermal-sprayed Ni50Cr coatings, J. Therm. Spray Technol. 26 (2017) 554–568, https://doi.org/10.1007/s11666-017-0531-z.

[52] G.C. Wood, B. Chattopadhyay, Transient oxidation of Ni-base alloys, Corros. Sci. 10 (1970) 471–480, https://doi.org/10.1016/S0010-938X(70)80032-4.

[53] V. Hastak, E.J. Gildersleeve, S. Batna, A.S. Gandhi, S. Sampath, On the oxygen vacancy annealing in air plasma sprayed yttria-stabilized zirconia thermal barrier coatings, J. Am. Ceram. Soc. 107 (2024) 920–932, https://doi.org/10.1111/jace.19477.

[54] A. Killinger, P. Müller, R. Gadow, What do we know, what are the current limitations of suspension HVOF spraying? J. Therm. Spray Technol. 24 (2015) 1130–1142, https://doi.org/10.1007/s11666-015-0264-9.

[55] R.N. Walters, S.M. Hackett, R.E. Lyon, Heats of combustion of high temperature polymers, Fire Mater. 24 (2000) 245–252, https://doi.org/10.1002/1099-1018(200009/10)24:5<245::AID-FAM744>3.0.CO;2-7.

[56] A. Sharma, R. Gambino, S. Sampath, Anisotropic electrical properties in thermal spray metallic coatings, Acta Mater. (2005) S1359645405004970, https://doi.org/10.1016/j.actamat.2005.08.029.

[57] A. Valarezo, S. Sampath, An integrated assessment of process-microstructure-property relationships for thermal-sprayed NiCr coatings, J. Therm. Spray Technol. 20 (2011) 1244–1258, https://doi.org/10.1007/s11666-011-9665-6.

[58] S. Brossard, P.R. Munroe, M.M. Hyland, Study of the splat formation for HVOF sprayed NiCr on stainless steel substrates and the effects of heating and boiling pre-treatments, J. Therm. Spray Technol. 19 (2010) 990–1000, https://doi.org/10.1007/s11666-010-9502-3.

[59] R.W. Powell, Correlation of the thermal and electrical conductivity of metals, alloys and compounds, in: Proceed. Confer. On Thermal Conductivity, 1963, pp. 79–112.

[60] Yu.V. Glagoleva, N.B. Pushkareva, Yu.E. Lapshova, O.V. Sadyreva, V.F. Polev, V. I. Gorbatov, S.G. Taluts, I.G. Korshunov, Thermophysical and transport properties of nickel-chromium alloys at high temperatures, Phys. Metals Metallogr. 102 (2006) 48–54, https://doi.org/10.1134/S0031918X06070064.

[61] S. Chandra, P. Fauchais, Formation of solid splats during thermal spray deposition, J. Therm. Spray Technol. 18 (2009) 148–180, https://doi.org/10.1007/s11666-009-9294-5.

[62] M. Vardelle, A. Vardelle, A.C. Leger, P. Fauchais, D. Gobin, Influence of particle parameters at impact on splat formation and solidification in plasma spraying processes, JTST 4 (1995) 50–58, https://doi.org/10.1007/BF02648528.

[63] S. Deshpande, S. Sampath, H. Zhang, Mechanisms of oxidation and its role in microstructural evolution of metallic thermal spray coatings—case study for Ni–Al, Surf. Coat. Technol. 200 (2006) 5395–5406, https://doi.org/10.1016/j.surfcoat.2005.07.072.

[64] R. Dhiman, A.G. McDonald, S. Chandra, Predicting splat morphology in a thermal spray process, Surf. Coat. Technol. 201 (2007) 7789–7801, https://doi.org/10.1016/j.surfcoat.2007.03.010.

[65] G. Mittal, S. Paul, Suspension and solution precursor plasma and HVOF spray: a review, J. Therm. Spray Technol. 31 (2022) 1443–1475, https://doi.org/10.1007/s11666-022-01360-w.

[66] P. Fauchais, M. Vardelle, J.F. Coudert, A. Vardelle, C. Delbos, J. Fazilleau, Thermal plasma deposition from thick to thin coatings and from micro- to nanostructure, Pure Appl. Chem. 77 (2005) 475–485, https://doi.org/10.1351/pac200577020475.

[67] G. Bolelli, C. Vorkötter, L. Lusvarghi, S. Morelli, V. Testa, R. Vaßen, Performance of wear resistant MCrAlY coatings with oxide dispersion strengthening, Wear 444–445 (2020) 203116, https://doi.org/10.1016/j.wear.2019.203116.

[68] C. Vorkötter, D.E. Mack, D. Zhou, O. Guillon, R. Vaßen, Effect of low-CTE oxide-dispersion-strengthened bond coats on columnar-structured YSZ coatings, Coatings 12 (2022) 396, https://doi.org/10.3390/coatings12030396.

[69] N. Branland, E. Meillot, P. Fauchais, A. Vardelle, F. Gitzhofer, M. Boulos, Relationships between microstructure and electrical properties of RF and DC plasma-sprayed titania coatings, J. Therm. Spray Technol. 15 (2006) 53–62, https://doi.org/10.1361/105996306X92596.

[70] F.G. Cuevas, J.M. Montes, J. Cintas, P. Urban, Electrical conductivity and porosity relationship in metal foams, J. Porous. Mater. 16 (2009) 675–681, https://doi.org/10.1007/s10934-008-9248-1.

[71] R.A. Rapp, Kinetics, microstructures and mechanism of internal oxidation - its effect and prevention in high temperature alloy oxidation, Corrosion 21 (1965) 382–401, https://doi.org/10.5006/0010-9312-21.12.382.

[72] F.H. Stott, G.C. Wood, Internal oxidation, Mater. Sci. Technol. 4 (1988) 1072–1078, https://doi.org/10.1179/mst.1988.4.12.1072.

[73] Improvements in high temperature oxidation resistance by additions of reactive elements or oxide dispersions, Phil. Trans. R. Soc. Lond. A 295 (1980) 309–329, https://doi.org/10.1098/rsta.1980.0124.

[74] H. Wang, J. Guo, S. Lei, W. Li, X. Zhang, Unveiling the formation of oxide layers on Ni-16Cr and Ni-20Cr alloys by the addition of Ta, J. Alloys Compd. 965 (2023) 171361, https://doi.org/10.1016/j.jallcom.2023.171361.

[75] Electrical heating fundamentals, in: The Efficient Use of Energy, Elsevier, 1982, pp. 94–114, https://doi.org/10.1016/B978-0-408-01250-8.50016-7.